Earth-Abundant Transition Metal Oxides with Extraordinary Oxygen Exchange Capacity for Efficient Thermochemical Synthesis of Solar Fuels

Xiang Gao,[a] Guanyu Liu,[a] Ye Zhu,[b] Peter Kreider,[c] Alicia Bayon,[d] Thomas Gengenbach,[e] Jim Hinkley,[d] Wojciech Lipiński*[c] and Antonio Tricoli*[a]

[a]*Nanotechnology Research Laboratory, Research School of Engineering, The Australian National University, Canberra, ACT 2601, Australia. E-mail: antonio.tricoli@anu.edu.au; Tel: +61 2 612 51696*

[b]*Department of Applied Physics, The Hong Kong Polytechnic University, Hung Hom, Kowloon, Hong Kong*

[c]*Solar Thermal Group, Research School of Engineering, The Australian National University, Canberra, ACT 2601, Australia. E-mail: wojciech.lipinski@anu.edu.au; Tel: +61 2 612 57896*

[d]*CSIRO Energy, P. O. Box 330, Newcastle, NSW 2300, Australia*

[e]*CSIRO Manufacturing, Bayview Avenue, Melbourne, VIC 3168, Australia*

Keywords: Solar Fuels, Transition Metal Carbides, Redox Materials, Oxygen Exchange Capacity, Earth-Abundant Transition Metals, Thermochemical

Abstract

Efficient storage of solar and wind power is one of the most challenging tasks still limiting the utilization of the prime but intermittent renewable energy sources. The direct storage of concentrated solar power in renewable fuels via thermochemical splitting of water and carbon dioxide on a redox material is a scalable approach with up to 54% solar-to-fuel conversion efficiency. Despite progress, the search for earth-abundant materials that can provide and maintain high H_2 and CO production rates over hundreds of high-temperature cycles continues. Here, we report a strategy to unlock the use of manganese, the 12th most abundant element in the Earth's crust, for thermochemical synthesis of solar fuels, achieving superior thermochemical stability, oxygen exchange capacity, and up to seven times higher mass-specific H_2 and CO yield than cerium dioxide. We observe that incorporation of a small fraction of cerium ions in the manganese (II,III) oxide crystal lattice drastically increases its oxygen ion mobility, allowing its reduction from oxide to carbide during methane partial oxidation with simultaneous Ce exsolution. High CO_2 and H_2O splitting rates are achieved by re-oxidation of the carbide to manganese (II) oxide with simultaneous reincorporation of the cerium ions. We demonstrate that the oxide to carbide reaction is highly reversible achieving remarkable CO_2 splitting rates over more than 100 thermochemical cycles of methane partial oxidation and CO_2 splitting, and preserving the initial oxygen exchange capacity of 0.65 $mol_O\ mol_{Mn}^{-1}$ and 89% of the fuel production rates. More generally, these findings suggest that incorporation of small soluble amounts of cerium in earth-abundant transition metal oxides like manganese oxide is a powerful approach to enable solar thermochemical fuel synthesis.

Introduction

Reduction of anthropogenic carbon emissions is a pivotal task requiring significant progress in renewable energy conversion and storage technologies. Direct synthesis of renewable fuels via solar thermochemical splitting of water and carbon dioxide can enable the use of this prime renewable energy source for transport, off-the-grid power generation and storage as well as production of numerous commodities.[1,2] Extensive efforts have been devoted to find efficient processes that can reduce the excessively high temperatures (> 3300 K) required for direct thermal dissociation of CO_2 and H_2O into CO, H_2 and O_2, and facilitate the separation of these gases.[3,4] Two-step reduction-oxidation (redox) cycles using a metal oxide as an intermediate oxygen exchange material are one of the most promising processes for large-scale water and carbon dioxide splitting.[4-6] Recently, it was shown that by promoting the reduction of the metal oxide material with methane partial oxidation (MPO) rather than by inert gas sweeping (IGS), it is possible to decrease the required reaction temperature from 1600 K to less than 1200 K.[1,7,8] This MPO-driven metal oxide reduction also increases the solar-to-fuel conversion efficiency limit from 19% for the IGS-driven cycles to 54%.[3,8-10] Notably, the resulting CO and H_2 products can be adjusted to match the required composition ratio for production and downstream processing of syngas, providing a simple pathway for large-scale synthesis of liquid fuels via established industrial solutions such as the Fischer–Tropsch process. MPO-driven H_2O or CO_2 splitting redox cycles are closely related to the industrial methane reforming processes but with important advantages that can overcome some of the main limitations of traditional steam reforming (Eq. 1) or dry reforming methods (Eq. 2).

$$CH_4 + H_2O \rightarrow 3\ H_2 + CO,\ \Delta H^o_{298} = +206\ \text{kJ mol}^{-1} \quad (1)$$

$$CH_4 + CO_2 \rightarrow 2\ H_2 + 2\ CO,\ \Delta H^o_{298} = +247\ \text{kJ mol}^{-1} \quad (2)$$

Currently, only steam methane reforming has been commercialized. In the US, it accounts for more than 95% production of the hydrogen.[11] Notably, the heat for the required processes is commonly supplied by gas heaters that burn up to 41% of the methane feedstock to maintain the temperature of the endothermic catalytic reaction.[1,11] This results in a 24% reduction in energy content compared to the initial feedstock[10]. Utilizing concentrated solar energy to drive methane reforming processes can completely supplement that

fossil-fuel energy demands to run the process and simultaneously store solar energy in the chemical energy in the product stream. This solar methane upgrading process can reduce carbon emissions by 41% and store up to 28% of solar energy as chemical potential.[10-12]

Overall, one of the main issues with the steam and dry methane reforming process is that they do not result in a H_2/CO ratio of 2, which is required for the subsequent Fischer-Tropsch synthesis of liquid fuels, but in a H_2/CO ratio of 3 and 1 (Eq. 1, 2), respectively. As a result, the steam methane reforming process needs to be operated at 15-35 bar,[13] and the product gases have to go through additional water-gas shift reactions, commonly performed downstream through two additional reactors operated at 583-723 K and 483-513 K[14]. Furthermore, efficient and carbon-resistant catalysts for steam and dry reforming are based on noble metals resulting in significant costs.[15-20] As an economic compromise, catalysts in commercial steam reforming plants are Ni-based and suffer from relatively rapid deactivation and poor selectivity for methane partial oxidation to CO and H_2 versus full oxidation to CO_2 and H_2O.[21-27] In order to mitigate catalyst deactivation, conventional steam reformers must operate with excess oxidizer with a H_2O/CH_4 ratio ≥ 3[11], as opposed to a ratio of 1 suggested by Eq. 1. The parasitic energy requirement to evaporate and heat the extra water for reforming and water gas shift is significant (ca. 15% extra energy)[11]. Investigation of other low-cost transition metal based catalysts has not yielded a commercially viable substitute to Ni-based catalysts.[27] The commercial Ni-based catalysts suffer from sintering and coking,[28-31] which make them not very suitable for solar thermochemical processes, where large variations of temperature and pressure are common due to intermittent and inconsistent solar thermal loads. Variations of temperature and pressure are particularly problematic for gas-gas reactions such as steam methane reforming as they change the equilibrium conditions and essentially product H_2/CO ratios during operation.[1]

Two step thermochemical redox cycles, such as the one demonstrated in this work, have been proposed as alternatives to traditional methane reforming to improve product composition (H_2/CO) under variable solar thermal loads and to increase process viability. These thermochemical redox reforming processes are sometimes referred to as chemical-looping reforming (CLR) processes and can provide enhanced selectivity of 93% to CO and H_2 synthesis vs 74% for steam reforming,[32-36] can potentially circumvent

the energy-demanding downstream water gas shift steps by tuning the H_2/CO ratio in each step,[10,11] and typically showcase reduced carbon deposition and conversion of deposited carbon to CO.[1,10,37,38] The CLR process also has the potential to achieve up to 55% energy requirement reductions compared to traditional steam methane reforming.[12] These considerations make the chemical-looping reforming of methane a strong candidate for near-term fossil and bio-sourced methane processing.

A major challenge of solar thermochemical redox cycles is the search for earth-abundant low-cost materials that can provide high oxygen exchange capacity and fast fuel production rates over thousands of high temperature cycles in harsh environmental conditions. Many binary, ternary, and complex oxides such as ferries and perovskites have been explored, with the highest performing materials including CeO_2,[32,39,40] $Ce_xZr_{1-x}O_2$[41], $FeAl_2O_4$[42] and $La_xSr_{1-x}Mn_yAl_{1-y}O_3$[43-45]. Nanostructured cerium dioxide (CeO_2) remains the benchmark material for thermochemical cycles, featuring high mass-specific production rates of H_2 and CO.[32] Despite the fast reaction kinetics, CeO_2 provides only low oxygen exchange capacities of below 0.25 mol_O mol_{Ce}^{-1}.[8,32] Additionally, CeO_2 has been reported to suffer from significant deactivation after only a few cycles at moderate temperatures (1173 K)[32]. Enhancement of the initial oxygen exchange capacity by using support materials such as MgO has resulted in a maximum of only 0.43 mol_O mol_{Ce}^{-1} at 1273 K.[39] Since the oxygen exchange capacity provides the upper limit for the fuel production of each cycle, it is critical to develop materials that provide and maintain higher oxygen exchange capacity than CeO_2 in harsh thermochemical environments. In addition, cerium is a rare earth element, and while it is the most abundant of the lanthanides with a content in the Earth's crust of around 70 ppm, its extraction from natural deposits is laborious posing limitations for its future use in such large-scale energy conversion processes.

In search of higher oxygen exchange capacities and more earth-abundant cations, numerous transition metals have been explored as alternative to cerium, including $BaMn_xFe_{1-x}O_3$,[43] $Ni_xFe_{3-x}O_4$,[46] and $La_xSr_{1-x}MnO_3$[44]. Notwithstanding their extraordinary abundancy, iron-based metal oxides suffer from even faster deactivation than CeO_2.[43,47] As an alternative, manganese is the 12th most abundant element in the Earth's crust with a concentration of 1000 ppm, and its oxides can be readily obtained by refining low-cost minerals such as pyrolusite and hausmannite.[48-50] Small fractions of manganese ions have been

incorporated into benchmark metal oxides, such as CeO_2[51] and perovskites[45], demonstrating improved oxygen exchange capacity and overall H_2 yield in thermochemical water splitting.[51] However, there are currently no studies reporting the direct use of manganese oxide for thermochemical water or CO_2 splitting, due to thermodynamic limitations. An indirect three-step cycle for H_2 generation was demonstrated by utilizing MnO and NaOH, subsequent hydrolysis of the birnessite mineral phase to generate Mn_2O_3 and regenerate NaOH, followed by high-temperature reduction of Mn_2O_3 to MnO.[52-56] The latter approach suffers from energy losses due to the significant temperature swings (ca. 750 K) between the reduction and the hydrolysis steps and incomplete recovery of sodium during hydrolysis.

Here, we present a strategy to enhance the reaction rates and drastically increase the oxygen exchange capacity of manganese oxide, unlocking its use for efficient direct synthesis of solar fuels. We have observed that the incorporation of soluble amounts of cerium ions in manganese oxide enables its reduction to manganese carbide with an extraordinary theoretical oxygen exchange capacity of one mole of oxygen per mole of manganese. Thereafter, the significant oxidation enthalpy of the carbide can be utilized to drive the carbon dioxide and water splitting reactions with unprecedentedly high CO and H_2 yields. We hypothesise that incorporation of the cerium ions drastically increases the oxygen ion mobility in the manganese oxide lattice enabling the thermodynamically favourable formation of an intermediate transition metal carbide, and its re-oxidation during water and carbon dioxide splitting. Importantly, while the cerium exsolutes during the reduction step, it is fully reincorporated during the oxidation step allowing long-term cyclability. We demonstrate the potential of this material by the production of valuable syngas, a mixture of CO and H_2, at record-high yields over more than 100 CO_2 splitting cycles with harsh methane-driven reduction steps. We believe that these findings may be applied to many members of the large family of earth-abundant transition metals setting the basis to overcome one of the longstanding challenges for the efficient thermochemical synthesis of solar fuels.

Experimental

Synthesis of Nanostructures

The ultra-fine pure Mn_3O_4 and 3% (atomic) Ce-doped Mn_3O_4 (3% Ce Mn_3O_4) nanoparticles were synthesised using a custom built flame spray pyrolysis setup[32,57,58]. The precursor liquid solution for

synthesising pure Mn_3O_4 was prepared by dissolving manganese (III) acetylacetonate (Sigma Aldrich, technical grade) in 2-ethylhexanoic acid (Sigma Aldrich, purity ≥ 99%) with a total atomic concentration of Mn ions at 0.4 mol L^{-1}. Similarly, the precursor solution for synthesising 3% Ce Mn_3O_4 was prepared by mixing cerium (III) acetate hydrate (Sigma Aldrich, purity 99.9%) with manganese acetylacetonate at a Ce:Mn atomic ratio of 3:97, and dissolving the mixture in 2-ethylhexanoic acid with a total atomic concentration of the metal ions at 0.4 mol L^{-1}. Both solutions were heated in 368 K oil bath and subsequently added with equal volumetric amount of xylene to reach a total metal ion concentration of 0.2 mol L^{-1}. The final combustible solutions were fed at 5 mL min^{-1} rate through a custom-built nozzle, and atomised with an oxygen flow of 5 SLPM (grade 4.0) with a pressure drop of ca. 4 bar. The resulting spray was ignited with a surrounding annular premixed methane (flow rate of 1.2 SLPM, grade 4.5) and oxygen (flow rate of 2 SLPM, grade 4.0) flame. Nanoparticle powders were collected with a vacuum pump (ICME Type M80B4) on water-cooled glass-fibre filters (Sartorius glass microfiber, 150 mm diameter) placed at ca. 40 cm height above the burner.

Setup for Methane Partial Oxidation and CO_2 Splitting Cycles

The cyclic MPO and CO_2 splitting performance of pure Mn_3O_4 and 3% Ce Mn_3O_4 is investigated in a vertical-tube reactor placed inside an infrared gold image furnace(P4C-VHT, Advance Riko) illustrated in a previous work[32]. The powder samples are packed between two pieces of 2 mm thick highly porous and temperature-resistant alumina-based fibres (ALBF-1, 97% Al_2O_3 and 3% SiO_2, ZIRCAR), located on-axis of an alumina tube. The thickness of the powder samples is varied between 1 mm and 2 mm, which allows for a nearly uniform temperature distribution. Gas flow rates are regulated by mass flow controllers (F-201CV, Bronkhorst) before being delivered through the top of the tube. Sample temperature is measured using an alumina sealed type-K thermocouple located directly under the packed samples. The composition of the product gases is continuously monitored by a quadrupole mass spectrometer (OmniStarTM GSD 320, Pfeiffer Vacuum). All gas volumes are reported at SATP conditions (298 K, 1 bar).

To find the effective redox stoichiometry of the materials, the tubular reactor was initially purged of air under a flow of pure Ar (grade 5.0) at room temperature. The reactor was then heated from ambient

room temperature to the optimised isothermal operating temperature of 1173 K at a ramp of 80 K min^{-1}. Subsequently, the sample was cyclically reduced by CH_4 (grade 4.5) and oxidized by CO_2 (grade 4.5). The reduction step was performed using a mixture of CH_4 in Ar (8 vol%) at a total flow rate of 250 mL min^{-1} for 90 min. Then the tube was purged with Ar (250 mL min^{-1}) for 10 min. The oxidation step was initiated by delivering a mixture of CO_2 in Ar (4 vol%) at a total flow rate of 250 mL min^{-1} for 75 min. The tube was again purged with Ar (250 mL min^{-1}) for 10 min before the next cycle began. The time set for the reduction steps was determined from preliminary tests by monitoring the instantaneous H_2:CO evolution ratios. As the deviation of the H_2:CO ratios caused by thermal cracking of CH_4 begins to dominate after ca. 120 min into the reduction step, it will compromise the credibility of the desirable products produced via the major redox reactions. Therefore, the full reduction of the samples was not investigated in this study. The subsequent oxidation steps were kept sufficiently long enough to reoxidize as much of the samples as possible.

To demonstrate the intermediate cyclic stability of 3% Ce Mn_3O_4, a 100-cycle 1173 K isothermal test with 6 min for reduction and 12 min for oxidation using the same input gas flow composition as above was performed. The Ar purge gas was increased to 500 mL min^{-1} and kept for 5 min after each reduction and oxidation step. Automated gas switch and flow rate control was operated using an in-house developed LabVIEW (National InstrumentsTM) application integrated with the mass flow controllers and pneumatically actuated valves (1315R, Swagelok). As a comparative study, commercial CeO_2 powders (Alfa Aesar, purity 99.995%) was also tested for 100 cycles with the same conditions.

Sample Characterisation

Samples were characterised before and after the cyclic MPO and CO_2 splitting tests. X-ray diffraction (XRD) was performed using a D2 phaser diffractometer (Bruker). Each sample powder was scanned using Cu Kα (1.54 Å) radiation source with an operating voltage of 30 kV and a current of 10 mA. The scanning rate of 0.75° min^{-1} was applied to record the XRD patterns in the 2θ range of 10–80° at an increment of 0.02°. The Scherrer equation was applied for the most intense peaks to determine the crystalline domain size. The quantitative analysis was performed based on parabolic fitting using pseudo-Voigt profile parameters.

Information of the particle morphology and lattice plane spacing was analysed using a high-resolution transmission electron microscope (HR-TEM, JEOL 2100F) operated at 200 kV. Samples were deposited on 200-mesh carbon-filmed copper grids for imaging. Primary particle size and lattice plane spacing were obtained via the image processing software ImageJ. Additional energy dispersive X-ray spectroscopy (EDX) was performed using the scanning transmission electron microscopy (STEM) mode on the JEOL 2100F. Elemental mapping was carried out by scanning a STEM probe over the area of interest and acquiring EDX spectra at every beam positions. Atomic resolution STEM imaging and electron energy loss spectroscopy (EELS) was carried out on an aberration-corrected FEI Titan STEM operated at 300 kV.

X-ray photoelectron spectroscopy (XPS) analysis was performed using an AXIS Nova spectrometer (Kratos Analytical Inc., Manchester, UK) with a monochromatic Al Kα source at a power of 180 W (15 kV × 12 mA) with a hemispherical analyser operating in the fixed analyser transmission mode and the standard aperture (analysis area: 0.3 mm × 0.7 mm). The total pressure in the main vacuum chamber during analysis was typically around 10^{-8} mbar. Samples were loaded into shallow wells of custom-built sample holders. One batch of each sample was prepared. Two different locations were analysed on each sample at a nominal photoelectron emission angle of 0º with respect to the surface normal. As the actual emission angle is ill-defined in the case of powders (ranging from 0º to 90º), the sampling depth may range from 0 nm to ca. 10 nm. Survey spectra were acquired at pass energy of 160 eV. To obtain more detailed information about chemical structure and oxidation states, high resolution spectra were recorded from individual peaks at 40 eV pass energy. Data processing was performed using CasaXPS processing software version 2.3.15 (Casa Software Ltd., Teignmouth, UK). All elements present were identified from survey spectra. Binding energies were referenced to the C 1s peak at 284.8 eV for aliphatic hydrocarbon.

The carbon content of the samples formed after the reduction and oxidation was evaluated by TG-DSC analysis in a STA8000 Simultaneous Thermal Analyser (PerkinElmer). Samples were calcined in air (100 mL min^{-1}) in the temperature range of 303 K to 1273 K at 5 K min^{-1}. Evolution of sample mass and heat flow were recorded.

Reaction Equilibrium and Thermodynamic Analysis

The proposed reactions and the equilibriums were evaluated using the FactSage thermochemical analysis software[59]. The databases used in the calculations include FACT pure substances (FactPS), oxides (FToxid, including solid solution phases[60]) and miscellaneous (FTmisc) databases. The Gibbs free energy change (ΔG) of each reaction as a function of the equilibrium temperature were calculated between 473 K and 1573 K. All ΔG values were normalised as per unit mol of Mn in each equation. To obtain the equilibrium composition as a function of the temperature, the initial products were set as the stoichiometric molar amount according to the reaction equations shown in Figure S1. All gases were treated as ideal gases under 1 bar.

Results and Discussion

To investigate the feasibility of doping the manganese oxide crystal lattice with cerium ions, composite nanoparticles with Ce concentration varying from 3% to 50% of the total metal atom content were synthesised by flame spray pyrolysis. The synthesis method was chosen as a scalable method capable of synthesizing high purity manganese oxide nanocrystals with well-controlled structural properties in one step.[49] All of the as-prepared nanocomposites consisted of Mn_3O_4 crystals with a mixed Mn(II) and Mn(III) oxidation state (Figure S1). Incorporation of up to 10% of Ce resulted in a solid solution with the Mn_3O_4 matrix, while further increasing the Ce content resulted in its segregation and formation of a separated CeO_2 crystal phase. Upon initial trials, it was found that the 3% Ce provided an optimal enhancement of the reduction and oxidation kinetics of the manganese oxide. This optimal composition was further comparatively investigated with the pure manganese oxide, and benchmarked against CeO_2.

Figure 1 shows a structural comparison of the as-prepared pure and 3% Ce Mn_3O_4 nanoparticles. Both materials show similar nanoscale morphology consisting of agglomerated quasi-spherical primary particles with an average diameter of 11.2 nm and a geometric standard deviation of 1.7 (Figure S3). High-resolution transmission electron microscopic (HR-TEM) analysis of these samples reveals similar hexagonally-shaped monocrystalline nanoparticles and exposed {101} facets for both materials (Figure 1a,b). However, while the fringe spacing of the pure Mn_3O_4 (Figure 1a, inset) matches well the 0.49 nm lattice spacing of the {101} Mn_3O_4 plane,[49,61] the 3% Ce one is broader (0.51 nm) suggesting a

distortion of the tetragonal hausmannite crystal structure (Figure 1b, inset). These results were further corroborated by X-ray diffraction (XRD) analysis of these samples, which confirms the same Mn_3O_4 phase (JCPDS No.24–0734) and average crystallite size of approx. 11 nm for both pure and 3% Ce Mn_3O_4, but a shift of the {101} plane spacing from 0.49 nm of the former to 0.51 nm of the latter. The successful incorporation of the cerium ions was confirmed by energy-dispersive X-ray spectroscopy (EDX) analysis (Figure 1e), showing characteristic Ce emission energies, in addition to the Mn, for the 3% Ce Mn_3O_4 samples. The EDX of the pure manganese oxide reveals only Mn, and the presence of carbon and copper from the TEM grid (Figure 1d). The increase in lattice spacing, observed in the Ce-doped samples, is tentatively attributed to the incorporation of the cerium ions that have larger ionic radii (Ce^{4+}: 0.097 nm; Ce^{3+}: 0.114 nm) than manganese (Mn^{4+}: 0.053 nm; Mn^{3+}: 0.065 nm; Mn^{2+}: 0.083 nm)[62].

The atomic distribution of the cerium ions was further investigated by annular dark-field imaging (ADF) and electron energy loss spectroscopy (EELS) analysis across the {110} plane of the Ce-doped samples. Figure 1f shows a high-resolution scanning transmission electron microscopic (HR-STEM) image of a monocrystalline 3% Ce Mn_3O_4 particle and a high-magnification (inset) of the lattice image matching well the Mn_3O_4 structure model at the <110> zone axis[49]. EELS line scanning (Figure 1h) and its associated ADF detection profile (Figure 1g) show localized and increased intensities, which are associated with the presence of the Ce dopants and further confirm the formation of a substitutional $(Mn_{0.97}Ce_{0.03})_3O_4$ solid solution with no detectable segregation or clustering of the Ce inside the grains. The oxidation state of the cerium ions and possible variation in the electronic structure of the Mn were investigated by X-ray photoelectron spectroscopy (Figure 2). The Ce 3d spectrum observable in the 3% Ce Mn_3O_4 samples confirms the presence of tetravalent cerium (Figure 2a). In particular, the Ce^{4+} oxidation state is associated with a dominant peak at 917.0 eV.[63] The same spectrum with the broad Mn LMM Auger peak subtracted in the same spectral region (875 – 925 eV binding energy) to present the pure Ce 3d spectrum is shown in Figure S5. The Ce^{4+} presence in the Mn_3O_4 lattice appears to decrease the oxidation state of the manganese cations; this partial reduction of Mn is evidenced by a stronger intensity contribution to the Mn 2p spectrum at lower binding energy (641 eV; Figure 2b), and an

increased multiplet splitting of the Mn 3s doublet (Figure 2c).[64] It is hypothesised that the cerium ions may act as electron donor weakening the Mn-O bonds.

To investigate the overall impact of these structural reorganization on the oxygen exchange capacity and redox kinetics of the manganese oxide matrix, four sequential reduction and oxidation cycles were conducted comparatively with the pure and 3% doped manganese oxide (Figure 3a,b). To increase the overall solar-to-fuel efficiency limit and decrease the required reaction temperature, methane partial oxidation was utilized in the reduction step. A temperature of 1173 K was chosen as close to the lowest (1150 K) possible for the thermodynamically favourable partial oxidation of methane with small amount of CH_4 cracking and carbon formation (Figures S2a, c). Furthermore, this is also a suitable temperature to activate the subsequent exothermic oxidation step allowing the execution of the whole two-step cycle isothermally.[65-67] This decreases thermal losses that are associated with the temperature swings, required with inert gas reduction steps.[42] The re-oxidation kinetics was investigated in detail for CO_2 splitting (Figure 3a,b), and further validated also for H_2O splitting (Figure 3c). The overall thermodynamic reaction stoichiometry for this redox cycle (Figure S2) indicates favourable formation of manganese carbide (Mn_7C_3) by methane partial oxidation in the first step (Eq. 3, 4), and complete re-oxidation to manganese (II) oxide by CO_2 splitting during the second step (Eq. 5):[68-70]

$$Mn_3O_4 + CH_4 \rightarrow 3\ MnO + CO + 2\ H_2,\ \Delta H^o_{298} = +196.1\ kJ\ mol^{-1} \quad (3)$$

$$7\ MnO + 10\ CH_4 \rightarrow Mn_7C_3 + 7\ CO + 20\ H_2,\ \Delta H^o_{298} = +2557.7\ kJ\ mol^{-1} \quad (4)$$

$$Mn_7C_3 + 10\ CO_2 \rightarrow 7\ MnO + 13\ CO,\ \Delta H^o_{298} = -84.4\ kJ\ mol^{-1} \quad (5)$$

Notably, this alternative metal oxide to carbide redox cycle has a theoretical oxygen exchange capacity of 1 $mol_O\ mol_{Mn}^{-1}$ (Eq. 4). This is up to four times the maximum theoretical oxygen exchange capacity of pure ceria maintaining its cubic fluorite crystal structure[8,32]. A temporary oxygen exchange capacity of 0.378 was reported by reducing CeO_2 to Ce_2O_3, however, the CO_2 splitting rates decreased rapidly in the first two cycles.[40] The theoretical fuel production yields in this work are unprecedentedly high with 2.86 $mol_{H2}\ mol_{Mn}^{-1}$ and 1 $mol_{CO}\ mol_{Mn}^{-1}$ (Eq. 4) during methane partial oxidation. In comparison, the highest theoretical H_2 and CO yields from methane partial oxidation reported for cerium dioxide are 0.5 $mol_{H2}\ mol_{Ce}^{-1}$ and 0.25 $mol_{CO}\ mol_{Ce}^{-1}$. Similarly, the CO_2 splitting capacity during the oxidation step is 1.86

mol_{CO} mol_{Mn}^{-1} (Eq. 5) and thus more than 7 times higher than that achievable with cerium dioxide (0.25 mol_{CO} mol_{Ce}^{-1}).

Despite this favourable thermodynamics, Figure 3a shows that the pure Mn_3O_4 is unable to perform this oxide–carbide redox cycle (Eq. 3-5) and only demonstrates small amounts of H_2 and CO during the reduction step (< 0.32 mol_{H2} mol_{Mn}^{-1} and 0.16 mol_{CO} mol_{Mn}^{-1}), and CO during oxidation step (< 0.24 mol_{CO} mol_{Mn}^{-1}). More specifically, in the first reduction cycle with the pure Mn_3O_4, production of a small amount of CO and CO_2 was simultaneously observed after 5 min, while detectable H_2 was only measured after 45 min and accompanied by a distinct increase in CO production rate. Evolution of CO_2 is an undesirable side reaction indicating complete oxidation of methane. In the subsequent reduction cycles, the amount of evolved CO_2 decreased rapidly. These reduction profiles suggest that while a certain amount of reduction from Mn_3O_4 into MnO and perhaps from MnO to Mn_7C_3 according to Eq. 3 and 4 may be occurring, the reaction rates are likely too slow to advance significantly. This was further supported by the CO evolution profiles during the oxidation steps. A very small and rapidly decreasing yield and production rate of CO was observed. Overall, these results further corroborate previous studies indicating that, despite its low-cost and earth-abundancy, pure manganese oxide cannot be efficiently employed for either IGS of MPO-driven thermochemical CO_2 and H_2O splitting cycles. In fact, the highest mass-specific CO production rate measured here with the pure Mn_3O_4 was 2.3×10^{-4} mol_{CO} g^{-1} min^{-1}, and thus 71% lower than that of the state-of-the-art CeO_2,[32] which at the same conditions reaches a CO production rate of 8×10^{-4} mol_{CO} g^{-1} min^{-1}.

Notably, incorporation of 3% cerium ions in the Mn_3O_4 matrix drastically enhanced reduction and oxidation kinetics, unlocking this promising metal oxide-carbide redox cycle (Eq. 4-5). Figure 3b shows four exemplary redox cycles with the 3% Ce Mn_3O_4. In the reduction steps, the onset of the H_2 and CO evolution was simultaneous and immediate. The H_2 and CO production rates peaked at 1.6×10^{-1} mol_{H2} mol_{Mn}^{-1} min^{-1} and 0.5×10^{-1} mol_{CO} mol_{Mn}^{-1} min^{-1}, respectively, upon 10 min into the first reduction step. These rates are more than 20 times higher than that achieved with the pure Mn_3O_4. After 35 min of the first reduction step, the production rates entered a tailing stage, stabilizing at 0.3×10^{-1} mol_{H2} mol_{Mn}^{-1} min^{-1} and 0.04×10^{-1} mol_{CO} mol_{Mn}^{-1} min^{-1}, respectively. The slight increasing tail of H_2 production during the

reduction steps (Figure 3b) is attributed to an increased selectivity toward methane partial oxidation to H_2 and CO over full oxidation to H_2O and CO_2 with increasing reduction time. This is possibly caused by the decline in oxygen partial pressure during reduction from the metal oxide to metal carbide. Another possible mechanism is methane cracking to carbon and H_2. The latter may also be facilitated by the lower oxygen content with the progress of the reduction step and may lead to an increase in H_2 production rate. In fact, a certain fraction of methane cracking is confirmed by the carbon deposits observed on the metal carbides by TGA and TEM (Figure 4c and f). Over the last 3 reduction steps, the peak rates decreased, while the tail production rates were quite stable resulting in an average of $0.22\pm0.01\times10^{-1}$ mol_{H2} mol_{Mn}^{-1} min^{-1} and $0.05\pm0.008\times10^{-1}$ mol_{CO} mol_{Mn}^{-1} min^{-1}, respectively. Furthermore, non-negligible production of CO_2 was only observed in the first cycle (Figure S6). The high CO/CO_2 production ratios show an inverse scenario to that observed for the pure Mn_3O_4. As summarized in Figure S6, increasing H_2 tail production rates accompanied by a fast decline in CO_2 evolution rates were observed over the 4 redox cycles, indicating an increased selectivity for methane partial over full oxidation. Neglecting the first cycle, the average H_2 and CO yields were 2.32 ± 0.21 mol_{H2} mol_{Mn}^{-1} and 0.52 ± 0.07 mol_{CO} mol_{Mn}^{-1}, and thus comparable to those (2.86 mol_{H2} mol_{Mn}^{-1} and 1 mol_{CO} mol_{Mn}^{-1}) expected for the complete metal oxide to carbide reaction (Eq. 4).

The CO_2 splitting kinetics of the reduced Ce-doped manganese oxide showed fast CO evolution profiles with sharp initial peaks and sustained tail rates. While the peak CO production rate decreased from 0.7×10^{-1} to 0.5×10^{-1} mol_{CO} mol_{Mn}^{-1} min^{-1} from the first to the fourth cycle, the tail production rates were quite stable at $0.2\pm0.02\times10^{-1}$ mol_{CO} mol_{Mn}^{-1} min^{-1}. In line with the reduction steps, these CO production rates were also more than one order of magnitude higher than that of the pure manganese oxide. The average CO yield of 1.44 ± 0.04 mol_{CO} mol_{Mn}^{-1} in the last three CO_2 splitting steps is also comparable to that of 1.86 mol_{CO} mol_{Mn}^{-1} expected from complete re-oxidation of the carbide to the metal oxide (Eq. 5), suggesting successful completion of the redox cycle. Notably, the mass-specific CO yield of this 3% Ce Mn_3O_4 was 8 times higher than cerium dioxide,[32] while featuring comparable CO_2 splitting kinetics.

To understand the role of the cerium ions in enhancing the redox kinetics and overall thermochemical performance of manganese oxide, the structural properties of the pure and 3% Ce Mn_3O_4 were mapped along the four two-step cycles. The evolution of the XRD patterns reveals that while presenting the same crystal phase, particle size and nanoscale morphology, these two materials have very distinct redox behaviours (Figure 4a,b). As suggested by the H_2 and CO evolution profiles (Figure 3a), the quantitative XRD analysis confirms that the pure Mn_3O_4 fails to complete its reduction to metal carbide. Upon the first reduction step only 14 wt% of Mn_7C_3 is formed, while the residual 86 wt% is slightly reduced to MnO. During the first CO_2 splitting step, this Mn_7C_3-MnO composite is partially re-oxidized to 32 wt% Mn_3O_4 and 68 wt% MnO. However, after the fourth CO_2 splitting step, only MnO is present with no Mn_3O_4 formed. This indicates that while initially there is some cycling between Mn_3O_4 and MnO, this path is rapidly deactivated during the first few cycles. The deactivation of this path is attributed to the essential role of the nanoparticle surface for the Mn_3O_4-MnO redox cycle. As soon as the high specific surface area is lost due to sintering, the oxygen ions in the MnO lattice do not have enough mobility to re-oxidize it to Mn_3O_4. Furthermore, while this is the first demonstration of thermochemical syngas production with pure manganese oxide, the reduction from Mn_3O_4 to MnO (Eq. 3) has an oxygen exchange stoichiometry of only 0.33 $mol_O\ mol_{Mn}^{-1}$, and thus is not significantly higher than that of cerium dioxide (0.25 $mol_O\ mol_{Ce}^{-1}$). Here, we propose that the small amount of H_2 and CO evolved during the pure manganese oxide redox cycles arise mostly from the MnO to carbide pathway (Eq. 4 and 5). However, the poor mobility of the oxygen ions in the manganese oxide lattice limits the carbide formation to a small surface fraction, thus not allowing to attain the thermodynamic equilibrium (Figure S2c).

In stark contrast to the pure Mn_3O_4, upon the first reduction step, the XRD spectrum of the 3% Ce Mn_3O_4 reveals the presence of only Mn_7C_3 with no trace of MnO or other manganese oxides (Figure 4b). A small fraction of ca. 3-5 wt% CeO_2 and Ce_2O_3 was also detected observable in the XRD patterns, indicating exsolution of the cerium from the manganese carbide phase. After the first CO_2 splitting step, the manganese carbide was completely oxidized to MnO with no trace of segregated cerium oxides indicating its re-incorporation into the manganese oxide lattice. Notably, completion of the reduction and oxidation reactions were clearly observed also in the fourth cycle (Figure 4b), and explains the very high

H_2 and CO yields measured during the four redox cycles (Figure 3b). The thermodynamic feasibility of these results was assessed by comparing the Gibbs free energy of formation of possible reduction and oxidation reactions against the reaction temperature. The Ellingham diagram for the reduction (Figure S2a) shows spontaneous conversion of Mn_3O_4 into MnO under methane-rich environments. When Mn_3O_4 is completely consumed, MnO is spontaneously converted into Mn_7C_3 at temperatures above 1150 K (Eq. 4). For the re-oxidation by CO_2 splitting (Figure S2b), conversion from Mn_7C_3 to MnO (Eq. 5) is spontaneous, but further conversion from MnO to Mn_3O_4 is not thermodynamically favourable. Upon the first cycle starting from Mn_3O_4, this leads to the observed reversible MnO-Mn_7C_3 cycling described in Eq. 4 and Eq. 5. As a result, the MnO to Mn_7C_3 redox cycle is thermodynamically reversible and followed closely the dictated stoichiometry in Eq. 4-5. The unsatisfactory attempts to cycle the pure manganese oxides are attributed to kinetics constraints in line with the poor oxygen mobility in manganese oxides[71,72].

To verify the amount of manganese carbide formed, the pure and 3% Ce doped samples were analysed by thermogravimetric differential scanning calorimetry (TG-DSC) under calcination in air at 100 mL min^{-1}. Figure 4c shows the relative mass change and heat flow during air calcination of the pure and 3% Ce Mn_3O_4 after the fourth reduction step. Upon calcination in air a main Mn_2O_3 phase was detected for both the 3% Ce and pure Mn_3O_4 samples (Figure S4). Formation of Mn_2O_3 is in line with previous results obtained by calcination of nanostructured manganese oxide in air.[49] Most importantly, a mass loss was observed for both materials with increasing temperature from 800 to 870 K. This is in contrast to the expected mass gain due to oxidation from Mn_7C_3 or MnO to Mn_2O_3, which would lead to mass gains for the pure and 3% Ce Mn_3O_4 samples, respectively. This mass loss (Figure 4c) is attributed to the combustion of carbon deposits formed on the nanoparticle surface via methane cracking. An estimate of the mass balance based on the XRD compositions and gravimetric variations suggests that upon the fourth reduction the pure manganese oxide samples consisted of 17 wt% Mn_7C_3, 63 wt% MnO and 20 wt% carbon deposits. In contrast, the reduced 3% Ce Mn_3O_4 consisted of 58 wt% Mn_7C_3 and ca. 42 wt% carbon deposits. The TG-DSC analysis of the re-oxidized pure and 3% Ce Mn_3O_4 samples (Figure 4d) shows a smaller but noticeable mass loss of 8% and 3%, respectively, indicating that after 90 min in the oxidation cycle there are still some small amounts of carbon deposit (12-15 wt%). The initial mass gain is

attributed to the oxidation of MnO to higher valence states (first Mn_3O_4 and then Mn_2O_3) before the on-set (ca. 800-870 K) of the carbon deposits oxidation to CO_2. The latter mass loss overshadows the 11.3% increase in mass expected for oxidation of the MnO to the final Mn_2O_3, which was detected by XRD in the calcined samples (Fig. S4). Similar amount of methane cracking and carbon deposit have also been reported for the benchmark cerium dioxide in thermochemical CO_2 and H_2O splitting cycles with MPO reduction.[7,73,74] While carbon formation by methane cracking decreases the amount of CO produced in the reduction step, the CO deficit can be recovered in the oxidation step during CO_2 splitting by the reverse Boudouard reaction. Minimizing carbon formation and deposition can be pursued by optimizing the methane concentration, reaction temperature and cycle step time.[1]

Electron microscope analysis of the reduced 3% Ce Mn_3O_4 particles provides some further insights on the role of the cerium ions and the redox mechanism of these composites. After the fourth reduction step, the 3% Ce Mn_3O_4 particles have a segregated morphology composed of mostly nanoporous Mn-rich particles and some dense Ce domains (Figure 4e,f). The nanoporous domains are also rich in carbon, while the Ce domains are carbon free. These structures correspond well to the segregated manganese carbide and cerium dioxide crystal phases observed by XRD. Some segregated carbon is also identified outside of the Mn-containing particles. In line with the TGA analysis (Figure 4c), this is attributed to the carbon deposits formed via methane cracking. It is hypothesized that the cyclic migration of cerium ions in and out of the manganese domains results in a cyclic contraction and expansion of the crystal structure, which possibly results in a nanoporous morphology. The latter has extensive grain boundary and defects available for oxygen and reactant diffusion during the reduction and oxidation steps. This is supported by the strong 48% variation in crystal size of the 3% Ce Mn_3O_4 during the fourth cycle (Figure 4b) from 56 nm of the reduction to 83 nm of the oxidation steps. In comparison, the crystal size of the pure Mn_3O_4 varied only by ca. 2% from 100 nm to 102 nm between the reduction and oxidation steps (Figure 4a).

To evaluate the thermochemical stability of this material, the CO_2 splitting kinetics of the 3% Ce Mn_3O_4 was investigated over 100 continuous redox cycles with MPO-driven reduction. A comparative experiment was conducted with cerium dioxide to provide reference values for the overall material performance. Minimization of methane cracking was achieved by decreasing the reduction and oxidation

step times from 90 and 75 min (Figure 3) to 6 and 12 min. Figure 5a shows the H_2 and CO evolution rates for the 3% Ce Mn_3O_4 over these 100 redox cycles. After some initial oscillations and decline in peak CO production rate for both the reduction and oxidation step, the step-yields stabilized from the 50th cycle onward with an average yield of $3.5\pm0.07\times10^{-3}$ mol_{H2} g^{-1}, $0.8\pm0.08\times10^{-3}$ mol_{CO} g^{-1}, and $1\pm0.09\times10^{-3}$ mol_{CO} g^{-1} during methane partial oxidation and CO_2 splitting, respectively (Figure 5b). The initial decrease in the peak rates for methane partial oxidation and CO_2 splitting is attributed to the sintering of the nanoparticles, which decreases the available surface area slowing the reduction and oxidation kinetics. This initial surface area decrease is comparable to the behaviour observed with the nanostructured Mn_3O_4. However, the impact on the H_2 and CO yield is significantly smaller as the noteworthy bulk-diffusivity of the oxygen ions in both the 3% Ce Mn_3O_4 and CeO_2 keeps driving the redox reactions toward the thermodynamic equilibrium. The slight decline in performance can likely be mitigated by optimisation of the operating mode in a fluidised bed reactor or through the inclusion of a compatible secondary phase, as discussed in previous works[75,76].

Overall, the cerium-doped manganese oxide achieved 75% higher H_2 and 25% higher CO yields during the methane partial oxidation step and comparable yields during the CO_2 splitting step than the commercial CeO_2. The H_2 and CO production rates during the redox steps were comparable to those of CeO_2, which is the current benchmark material for fast redox reaction kinetics in thermochemical redox cycles. Table 2 reports a comparative summary of the cyclic performance of the 3% Ce Mn_3O_4 against that of commercial ceria and other high-performing materials reported for thermochemical CO_2 or H_2O splitting with inert gas and MPO-driven reductions. It should be noted that MPO-driven reduction is expected to lead to higher oxygen exchange capacity than inert gas reduction as recently reported for pure cerium dioxide.[32] Notably, the CO yield achieved here for CO_2 splitting is one order of magnitude higher than that of benchmark redox materials using inert gas reduction. This is also one of the highest CO production capacities from CO_2 splitting so far reported with an earth-abundant metal oxide material for thermochemical synthesis of solar fuels.

The long-term stability of the Ce-doped manganese oxide was further investigated by measuring the residual oxygen exchange capacity after the 100 redox cycles. Figure 5c and 5d show three MPO-driven

reduction and CO_2 splitting oxidation cycles for the cycled 3% Ce Mn_3O_4 and commercial CeO_2. Notably, the oxygen exchange capacity and H_2 and CO yields of the 3% Ce Mn_3O_4 was largely unchanged. The latter maintained comparable MPO and CO_2 splitting rates and yields to the as-prepared material (Figure 3). The 3% Ce revealed up to 7 and 5 times higher H_2 and CO yields, respectively, during the reduction steps, and 4–6 times higher CO yield during the CO_2 splitting steps than the commercial CeO_2. After 100 redox cycles, the oxygen exchange capacity of the Ce-doped manganese oxide, estimated from the average CO yield during the MPO steps, was 0.61 $mol_O\ mol_{Mn}^{-1}$ and thus close to the as-prepared material (0.65 $mol_O\ mol_{Mn}^{-1}$) despite an 81% decrease in specific surface area. This is attributed to the drastic improvement in oxygen ion mobility achieved by incorporation of the Ce^{4+} in the manganese oxide lattice, which may reduce the Mn-O binding energy and also create a microporous morphology. Further investigation of the manganese oxide to carbide cycles is required to provide a more robust assessment of its performance and comparison with other redox materials.

Conclusions

In conclusion, we believe that doping earth-abundant metal oxides with soluble amounts of high oxygen conductivity materials, such as cerium, may lead to a broadly applicable strategy to improve the redox kinetics and unlock the use of the outstanding oxygen exchange capacity of a broad family of low-cost materials for thermochemical processes with applications including solar fuel synthesis, fuel cells, and industrial fume and combustion engine exhaust treatments. The developed cerium-doped manganese oxide demonstrates the first metal oxide to carbide redox cycle and efficient use of manganese, one of the most earth-abundant elements, for high-temperature methane partial oxidation and carbon dioxide and water splitting. The incorporation of a fractional amount of cerium revealed markedly improved kinetics of the manganese oxide to manganese carbide redox reactions, resulting in 15 times higher CO_2 splitting rates than the undoped manganese oxide, and also 8 times higher CO yields than cerium oxide. The long-term cyclic performance revealed that this is not a short-lived enhancement and that the cerium ions are able to easily diffuse in and out of the host lattice over hundreds of reduction and oxidation cycles in harsh thermochemical conditions. As an immediate result, these findings provide a novel low-cost earth-

abundant material for use in methane reforming technologies and for the large-scale synthesis of solar fuels via efficient thermochemical routes.

Conflicts of Interest

There are no conflicts of interest to declare.

Acknowledgements

This research was partially funded by the Australian Solar Thermal Research Initiative (ASTRI) through the Australian Renewable Energy Agency (ARENA). Financial support from the ARC Discovery Project #150101939 and the ARC Discovery Early Career Award #160100569 (A. Tricoli), the ARC Future Fellowship FT140101213 (W. Lipiński), the Australian Government Research Training Program (X. Gao), and The Hong Kong Polytechnic University internal grant 1-ZE6G (Y. Zhu) is gratefully acknowledged. The microscopy analyses were conducted in the Centre of Advanced Microscopy at ANU, the University Research Facility in Materials Characterization and Device Fabrication (UMF) at the Hong Kong Polytechnic University, and Monash Centre for Electron Microscopy (MCEM) at Monash University. X. Gao would like to acknowledge N. Nasiri for the partial support of microscopy image acquisition and T. Tsuzuki for providing TG-DSC instruments. Y. Zhu is grateful to W. Lu for maintaining the JEOL 2100F TEM/STEM at UMF and M. Weyland for optimizing the Titan TEM/STEM at MCEM.

References

1. C. Agrafiotis, H. von Storch, M. Roeb and C. Sattler, *Renewable and Sustainable Energy Reviews*, 2014, **29**, 656-682.
2. R. Bader and W. Lipiński, in *Advances in Concentrating Solar Thermal Research and Technology*, ed. L. R. Santigosa, Woodhead Publishing, 2017, pp. 403-459.
3. W. C. Chueh, C. Falter, M. Abbott, D. Scipio, P. Furler, S. M. Haile and A. Steinfeld, *Science*, 2010, **330**, 1797-1801.
4. C. Agrafiotis, M. Roeb and C. Sattler, *Renewable and Sustainable Energy Reviews*, 2015, **42**, 254-285.
5. C. L. Muhich, B. D. Ehrhart, I. Al-Shankiti, B. J. Ward, C. B. Musgrave and A. W. Weimer, *Wiley Interdisciplinary Reviews: Energy and Environment*, 2016, **5**, 261-287.
6. A. Steinfeld, *Solar energy*, 2005, **78**, 603-615.
7. K. Otsuka, Y. Wang, E. Sunada and I. Yamanaka, *Journal of Catalysis*, 1998, **175**, 152-160.
8. P. T. Krenzke and J. H. Davidson, *Energy & Fuels*, 2014, **28**, 4088-4095.
9. R. Bader, L. J. Venstrom, J. H. Davidson and W. Lipiński, *Energy & Fuels*, 2013, **27**, 5533-5544.
10. P. T. Krenzke, J. R. Fosheim and J. H. Davidson, *Solar Energy*, 2017.
11. D. S. A. Simakov, M. M. Wright, S. Ahmed, E. M. A. Mokheimer and Y. Roman-Leshkov, *Catalysis Science & Technology*, 2015, **5**, 1991-2016.
12. A. Antzara, E. Heracleous, D. B. Bukur and A. A. Lemonidou, *International Journal of Greenhouse Gas Control*, 2015, **32**, 115-128.
13. M. C. Kung and H. H. Kung, *Surface Science*, 1981, **104**, 253-269.
14. T. L. LeValley, A. R. Richard and M. Fan, *International Journal of Hydrogen Energy*, 2014, **39**, 16983-17000.
15. S. C. Tsang, J. B. Claridge and M. L. H. Green, *Catalysis Today*, 1995, **23**, 3-15.
16. J. R. Rostrupnielsen and J. H. B. Hansen, *Journal of Catalysis*, 1993, **144**, 38-49.
17. J. Wei and E. Iglesia, *The Journal of Physical Chemistry B*, 2004, **108**, 4094-4103.

18. M. H. Halabi, M. H. J. M. de Croon, J. van der Schaaf, P. D. Cobden and J. C. Schouten, *Applied Catalysis A: General*, 2010, **389**, 68-79.

19. K. Kusakabe, K.-I. Sotowa, T. Eda and Y. Iwamoto, *Fuel Processing Technology*, 2004, **86**, 319-326.

20. J. G. Jakobsen, M. Jakobsen, I. Chorkendorff and J. Sehested, *Catalysis Letters*, 2010, **140**, 90-97.

21. H. Wu, V. La Parola, G. Pantaleo, F. Puleo, A. M. Venezia and L. F. Liotta, *Catalysts*, 2013, **3**, 563-583.

22. C. -J. Liu, J. Ye, J. Jiang and Y. Pan, *ChemCatChem*, 2011, **3**, 529-541.

23. S. D. Angeli, G. Monteleone, A. Giaconia and A. A. Lemonidou, *International Journal of Hydrogen Energy*, 2014, **39**, 1979-1997.

24. J.-S. Choi, K.-I. Moon, Y. G. Kim, J. S. Lee, C.-H. Kim and D. L. Trimm, *Catalysis Letters*, 1998, **52**, 43-47.

25. C. Crisafulli, S. Scirè, R. Maggiore, S. Minicò and S. Galvagno, *Catalysis Letters*, 1999, **59**, 21-26.

26. M. M. Barroso Quiroga and A. E. Castro Luna, *Industrial & engineering chemistry research*, 2007, **46**, 5265-5270.

27. S. Bhavsar and G. Veser, *RSC Advances*, 2014, **4**, 47254-47267.

28. J. W. Snoeck, G. F. Froment and M. Fowles, *Journal of Catalysis*, 1997, **169**, 250-262.

29. J.-W. Snoeck, G. Froment and M. Fowles, *Industrial & engineering chemistry research*, 2002, **41**, 4252-4265.

30. M. Annesini, V. Piemonte and L. Turchetti, *Chemical Engineering*, 2007, **11**, 21-26.

31. J. R. Rostrup-Nielsen, *Catalysis Today*, 1993, **18**, 305-324.

32. X. Gao, A. Vidal, A. Bayon, R. Bader, J. Hinkley, W. Lipinski and A. Tricoli, *Journal of Materials Chemistry A*, 2016, **4**, 9614-9624.

33. S. A. Paripatyadar and J. T. Richardson, *Solar Energy*, 1988, **41**, 475-485.

34. H. B. Do, J. T. Jang and G. Y. Han, *Journal of Solar Energy Engineering*, 2012, **134**, 041013-041013-041014.

35. A. Berman, R. K. Karn and M. Epstein, *Green Chemistry*, 2007, **9**, 626-631.

36. T. Kodama, Y. Isobe, Y. Kondoh, S. Yamaguchi and K. I. Shimizu, *Energy*, 2004, **29**, 895-903.

37. E. J. Sheu and A. F. Ghoniem, *International Journal of Hydrogen Energy*, 2014, **39**, 14817-14833.

38. E. J. Sheu, E. M. A. Mokheimer and A. F. Ghoniem, *International Journal of Hydrogen Energy*, 2015, **40**, 12929-12955.

39. P. T. Krenzke, J. R. Fosheim, J. Zheng and J. H. Davidson, *International Journal of Hydrogen Energy*, 2016, **41**, 12799-12811.

40. M. M. Nair and S. Abanades, *Energy & Fuels*, 2016, **30**, 6050-6058.

41. A. Le Gal, S. Abanades and G. Flamant, *Energy & Fuels*, 2011, **25**, 4836-4845.

42. C. L. Muhich, B. W. Evanko, K. C. Weston, P. Lichty, X. Liang, J. Martinek, C. B. Musgrave and A. W. Weimer, *Science*, 2013, **341**, 540-542.

43. A. Mishra, N. Galinsky, F. He, E. E. Santiso and F. Li, *Catalysis Science & Technology*, 2016, **6**, 4535-4544.

44. H. Wei, Y. Cao, W. Ji and C. Au, *Catalysis Communications*, 2008, **9**, 2509-2514.

45. A. H. McDaniel, E. C. Miller, D. Arifin, A. Ambrosini, E. N. Coker, R. O'Hayre, W. C. Chueh and J. Tong, *Energy & Environmental Science*, 2013, **6**, 2424-2428.

46. T. Kodama, T. Shimizu, T. Satoh, M. Nakata and K. I. Shimizu, *Solar Energy*, 2002, **73**, 363-374.

47. F. He, Y. Wei, H. Li and H. Wang, *Energy & Fuels*, 2009, **23**, 2095-2102.

48. M. Wiechen, M. Najafpour, S. Allakhverdiev and L. Spiccia, *Energy & Environmental Science*, 2014, **7**, 2203-2212.

49. G. Liu, J. Hall, N. Nasiri, T. Gengenbach, L. Spiccia, M. H. Cheah and A. Tricoli, *ChemSusChem*, 2015, **8**, 4162-4171.

50. F. Cheng, J. Shen, B. Peng, Y. Pan, Z. Tao and J. Chen, *Nat Chem*, 2011, **3**, 79-84.

51. H. Kaneko, T. Miura, H. Ishihara, S. Taku, T. Yokoyama, H. Nakajima and Y. Tamaura, *Energy*, 2007, **32**, 656-663.

52. T. M. Francis, P. R. Lichty and A. W. Weimer, *Chemical Engineering Science*, 2010, **65**, 3709-3717.

53. M. Sturzenegger, J. Ganz, P. Nüesch and T. Schelling, *Le Journal de Physique IV*, 1999, **9**, Pr3-331-Pr333-335.

54. P. B. Kreider, H. H. Funke, K. Cuche, M. Schmidt, A. Steinfeld and A. W. Weimer, *International Journal of Hydrogen Energy*, 2011, **36**, 7028-7037.

55. A. Bayón, V. A. de la Peña O'Shea, D. P. Serrano and J. M. Coronado, *International Journal of Hydrogen Energy*, 2013, **38**, 13143-13152.

56. A. Bayón, V. A. de la Peña O'Shea, J. M. Coronado and D. P. Serrano, *International Journal of Hydrogen Energy*, 2016, **41**, 113-122.

57. N. Nasiri, R. Bo, F. Wang, L. Fu and A. Tricoli, *Advanced Materials*, 2015, **27**, 4336-4343.

58. G. Liu, W. S. Wong, N. Nasiri and A. Tricoli, *Nanoscale*, 2016, **8**, 6085-6093.

59. C. W. Bale, E. Bélisle, P. Chartrand, S. A. Decterov, G. Eriksson, K. Hack, I. H. Jung, Y. B. Kang, J. Melançon, A. D. Pelton, C. Robelin and S. Petersen, *Calphad*, 2009, **33**, 295-311.

60. M. D. Allendorf, R. B. Diver, N. P. Siegel and J. E. Miller, *Energy & Fuels*, 2008, **22**, 4115-4124.

61. C.-C. Hu, Y.-T. Wu and K.-H. Chang, *Chemistry of Materials*, 2008, **20**, 2890-2894.

62. P. Zhang, H. Lu, Y. Zhou, L. Zhang, Z. Wu, S. Yang, H. Shi, Q. Zhu, Y. Chen and S. Dai, *Nature Communications*, 2015, **6**, 8446.

63. D. R. Mullins, S. H. Overbury and D. R. Huntley, *Surface Science*, 1998, **409**, 307-319.

64. M. C. Biesinger, B. P. Payne, A. P. Grosvenor, L. W. M. Lau, A. R. Gerson and R. S. C. Smart, *Applied Surface Science*, 2011, **257**, 2717-2730.

65. A. Serrano-Lotina and L. Daza, *International Journal of Hydrogen Energy*, 2014, **39**, 4089-4094.

66. K. Zhao, F. He, Z. Huang, A. Zheng, H. Li and Z. Zhao, *Chinese Journal of Catalysis*, 2014, **35**, 1196-1205.

67. A. Serrano-Lotina and L. Daza, *Applied Catalysis A: General*, 2014, **474**, 107-113.

68. N. Anacleto, O. Ostrovski and S. Ganguly, *ISIJ international*, 2004, **44**, 1480-1487.

69. O. Ostrovski and G. Zhang, *AIChE journal*, 2006, **52**, 300-310.

70. C. H. Eom and D. J. Min, *Metals and Materials International*, 2016, **22**, 129-135.

71. M. Nolan, J. E. Fearon and G. W. Watson, *Solid State Ionics*, 2006, **177**, 3069-3074.

72. G. Zhou, P. R. Shah and R. J. Gorte, *Catalysis Letters*, 2008, **120**, 191-197.

73. J. T. Jang, K. J. Yoon, J. W. Bae and G. Y. Han, *Solar Energy*, 2014, **109**, 70-81.

74. H. H. Jeong, J. H. Kwak, G. Y. Han and K. J. Yoon, *International Journal of Hydrogen Energy*, 2011, **36**, 15221-15230.

75. A. Shafiefarhood, J. C. Hamill, L. M. Neal and F. Li, *Physical Chemistry Chemical Physics*, 2015, **17**, 31297-31307.

76. N. L. Galinsky, A. Shafiefarhood, Y. Chen, L. Neal and F. Li, *Applied Catalysis B: Environmental*, 2015, **164**, 371-379.

77. K. Otsuka, Y. Wang and M. Nakamura, *Applied Catalysis A: General*, 1999, **183**, 317-324.

78. Z. Xing, W. Hua, W. Yonggang, L. Kongzhai and X. Cheng, *Journal of Rare Earths*, 2010, **28**, 907-913.

79. P. Furler, J. R. Scheffe and A. Steinfeld, *Energy & Environmental Science*, 2012, **5**, 6098-6103.

Table 1. Syngas yields and CO selectivity between pure Mn_3O_4 and 3% Ce Mn_3O_4 over 4 cycles of methane partial oxidation and CO_2 splitting.

Material	Cycle	Reduction (MPO)				Oxidation (CDS)
		H_2 yield [mol mol_{Mn}^{-1}]	CO yield [mol mol_{Mn}^{-1}]	CO_2 yield [mol mol_{Mn}^{-1}]	S_{CO} [%]	CO yield [mol mol_{Mn}^{-1}]
Mn_3O_4	1	0.22	0.16	0.17	48.4	0.24
	2	0.32	0.12	0.06	67.1	0.17
	3	0.21	0.07	0.02	78.3	0.12
	4	0.07	0.02	0.02	52.3	0.10
3% Ce Mn_3O_4	1	3.71	1.05	0.28	78.9	1.89
	2	2.09	0.56	0.07	88.8	1.39
	3	2.37	0.56	0.05	91.8	1.47
	4	2.51	0.43	0.03	93.4	1.46

Table 2. Comparison of syngas production in two-step thermochemical redox cycles.[a)]

Material	Process	t_c [h]	N_c [#]	Reduction			Oxidation			Ref.
				T_R [K]	Y_{H2} [10^{-3} mol g^{-1}]	Y_{CO} [10^{-3} mol g^{-1}]	T_O [K]	Y_{H2} [10^{-3} mol g^{-1}]	Y_{CO} [10^{-3} mol g^{-1}]	
3% Ce Mn_3O_4	MPO-CDS	46.7	100	1173	3.44	0.90	1173	--	1.30	This work
3% Ce Mn_3O_4	MPO-WS	2	2	1173	37.8	11.3	1173	11.2	3.63	This work
CeO_2	MPO-CDS	46.7	100	1173	1.97	0.72	1173	--	1.55	This work
$Ce_{0.8}Zr_{0.2}O_2$	MPO-WS	>2.7	1	973	1.29	0.62	773	0.84	--	Otsuka et al.[77]
$Ce_{0.7}Fe_{0.3}O_3$	MPO-WS	>6.3	10	1123	1.19	0.63	973	1.02	--	Xing et al.[78]
CeO_2/SiC	MPO-WS	0.7	3	1273	1.75	0.43	1273	1.22	--	Nair et al.[40]
CeO_2	IGS-WS	166.7	500	1773	--	--	1073	0.61	--	Chueh et al.[3]
CeO_2	IGS-WS+CDS	>8	10	1700	--	--	1100	0.09	0.04	Furler et al.[79]
SLMA2	IGS-CDS	40	80	1623	--	--	1273	--	0.14	McDaniel et al.[45]
Hercynite	IGS-WS	4.6	3	1623	--	--	1623	0.10	--	Muhich et al.[42]

[a)] t_c: operating time; N_c: number of cycles; T_R: reduction temperature; T_O: oxidation temperature; Y_{H2}: H_2 yield; Y_{CO}: CO yield; MPO: methane partial oxidation; CDS: carbon dioxide splitting; WS: water splitting; IGS: inert gas sweeping.

Captions

Figure 1. Morphological characterization of the cerium-doped manganese oxide. HR-TEM micrographs (a and b), XRD patterns (c) and EDX (d and e) of the as-prepared Pure and 3% Ce Mn_3O_4 nanostructures. HR-STEM micrograph (f) showing a primary 3% Ce Mn_3O_4 nanoparticle with associated ADF detection profile (g) and EELS (h) along the dotted line.

Figure 2. Structural characterization of the cerium-doped manganese oxide. XPS of the as-prepared Pure and 3% Ce Mn_3O_4 showing the characteristic spectra of (a) Ce 3d, (b) Mn 2p and (c) Mn 3s.

Figure 3. Efficient carbon dioxide splitting via the oxide-carbide cycle. H_2 and CO production rates of the (a) Pure and (b) 3% Ce Mn_3O_4 during 4 isothermal cycles of methane partial oxidation and CO_2 splitting at 1173 K. (c) H_2 and CO production rates of 3% Ce Mn_3O_4 during 2 isothermal cycles of methane partial oxidation and H_2O splitting at 1173 K.

Figure 4. Evolution of the cerium-doped manganese oxide composition during the redox cycles. XRD patterns of the (a) Pure and (b) 3% Ce Mn_3O_4 during the 1^{st} and 4^{th} cycles of methane partial oxidation and CO_2 splitting. TG-DSC analysis of calcination in air at 100 mL min^{-1} showing relative mass change and heat flow of the Pure and 3% Ce Mn_3O_4 after (c) the 4^{th} reduction step and (d) the 4^{th} oxidation step. STEM micrograph (e) showing nanoporous 3% Ce Mn_3O_4 after the 4^{th} reduction step and its associated elemental mapping (f) showing segregated carbon-rich Mn domains and carbon-free Ce domains.

Figure 5. Investigation of the mid-term CO_2 splitting kinetics and mid-term stability over consecutive 100 redox cycles. (a) H_2 and CO production rates of the 3% Ce Mn_3O_4 during 100 isothermal cycles of methane partial oxidation and CO_2 splitting and its (b) H_2 and CO yields in every 5^{th} cycle. H_2 and CO production rates of the (c) 3% Ce Mn_3O_4 and (d) commercial CeO_2 over 3 extended cycles after 100 cycles of methane partial oxidation and CO_2 splitting.

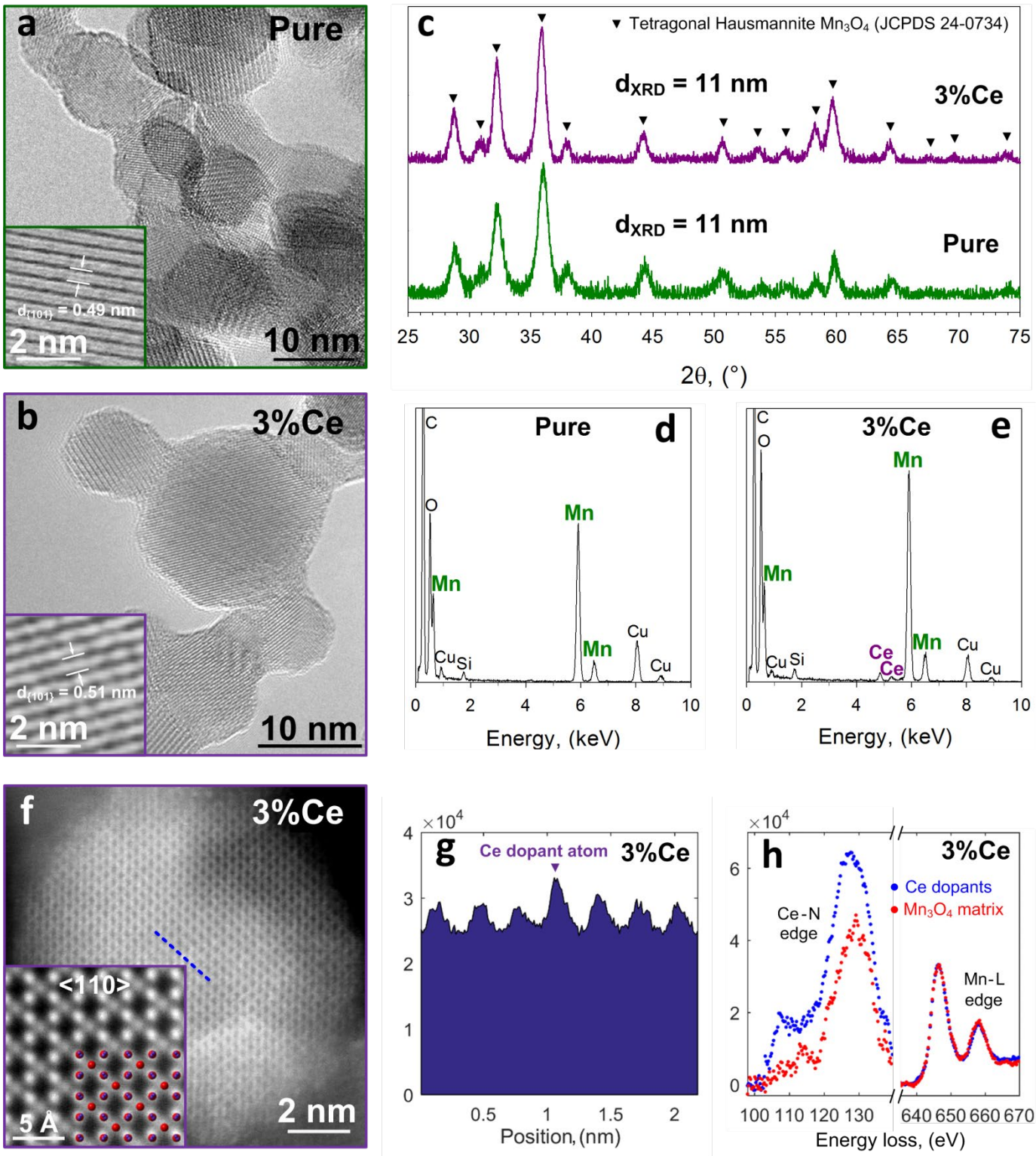
a
Pure
$d_{\{101\}}$ = 0.49 nm
2 nm
10 nm
b
3%Ce
$d_{\{101\}}$ = 0.51 nm
2 nm
10 nm
c
▼ Tetragonal Hausmannite Mn_3O_4 (JCPDS 24-0734)
d_{XRD} = 11 nm
3%Ce
d_{XRD} = 11 nm
Pure
25 30 35 40 45 50 55 60 65 70 75
2θ, (°)
d
Pure
C
O
Mn
Mn
Cu Si
Mn
Cu
Cu
0 2 4 6 8 10
Energy, (keV)
e
3%Ce
C
O
Mn
Mn
Cu Si
Ce
Ce
Mn
Cu
Cu
0 2 4 6 8 10
Energy, (keV)
f
3%Ce
<110>
5 Å
2 nm
g
Ce dopant atom
3%Ce
×10^4
4 3 2 1 0
0.5 1 1.5 2
Position, (nm)
h
3%Ce
×10^4
6 4 2 0
Ce dopants
Mn_3O_4 matrix
Ce-N edge
Mn-L edge
100 110 120 130
640 650 660 670
Energy loss, (eV)

Figure 1

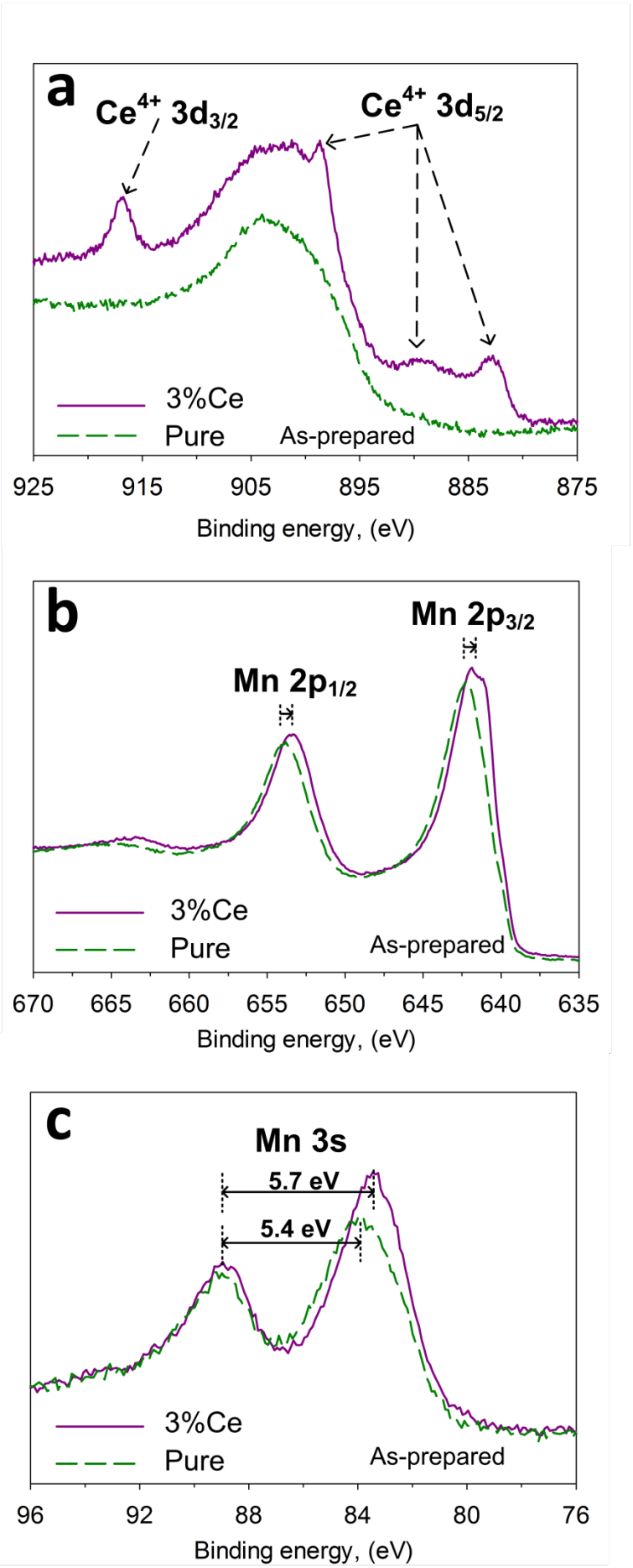
a
Ce4+ 3d3/2
Ce4+ 3d5/2
3%Ce
Pure
As-prepared
925
915
905
895
885
875
Binding energy, (eV)
b
Mn 2p3/2
Mn 2p1/2
3%Ce
Pure
As-prepared
670
665
660
655
650
645
640
635
Binding energy, (eV)
c
Mn 3s
5.7 eV
5.4 eV
3%Ce
Pure
As-prepared
96
92
88
84
80
76
Binding energy, (eV)

Figure 2

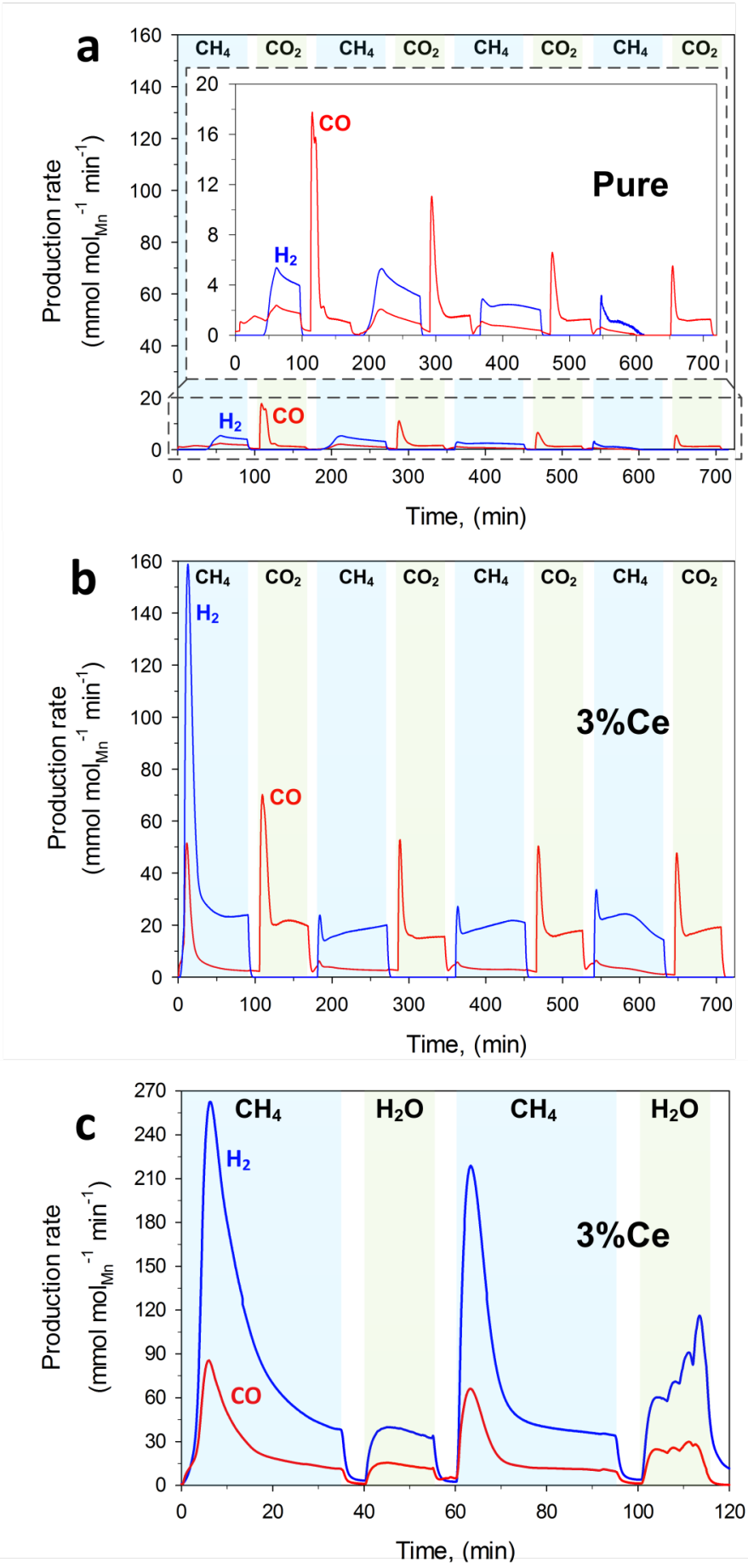
a
CH4
CO2
CH4
CO2
CH4
CO2
CH4
CO2
CO
H2
Pure
H2
CO
Production rate
(mmol mol$_{Mn}^{-1}$ min^{-1})
Time, (min)
b
CH4
CO2
CH4
CO2
CH4
CO2
CH4
CO2
H2
CO
3%Ce
Production rate
(mmol mol$_{Mn}^{-1}$ min^{-1})
Time, (min)
c
CH4
H2O
CH4
H2O
H2
CO
3%Ce
Production rate
(mmol mol$_{Mn}^{-1}$ min^{-1})
Time, (min)

Figure 3

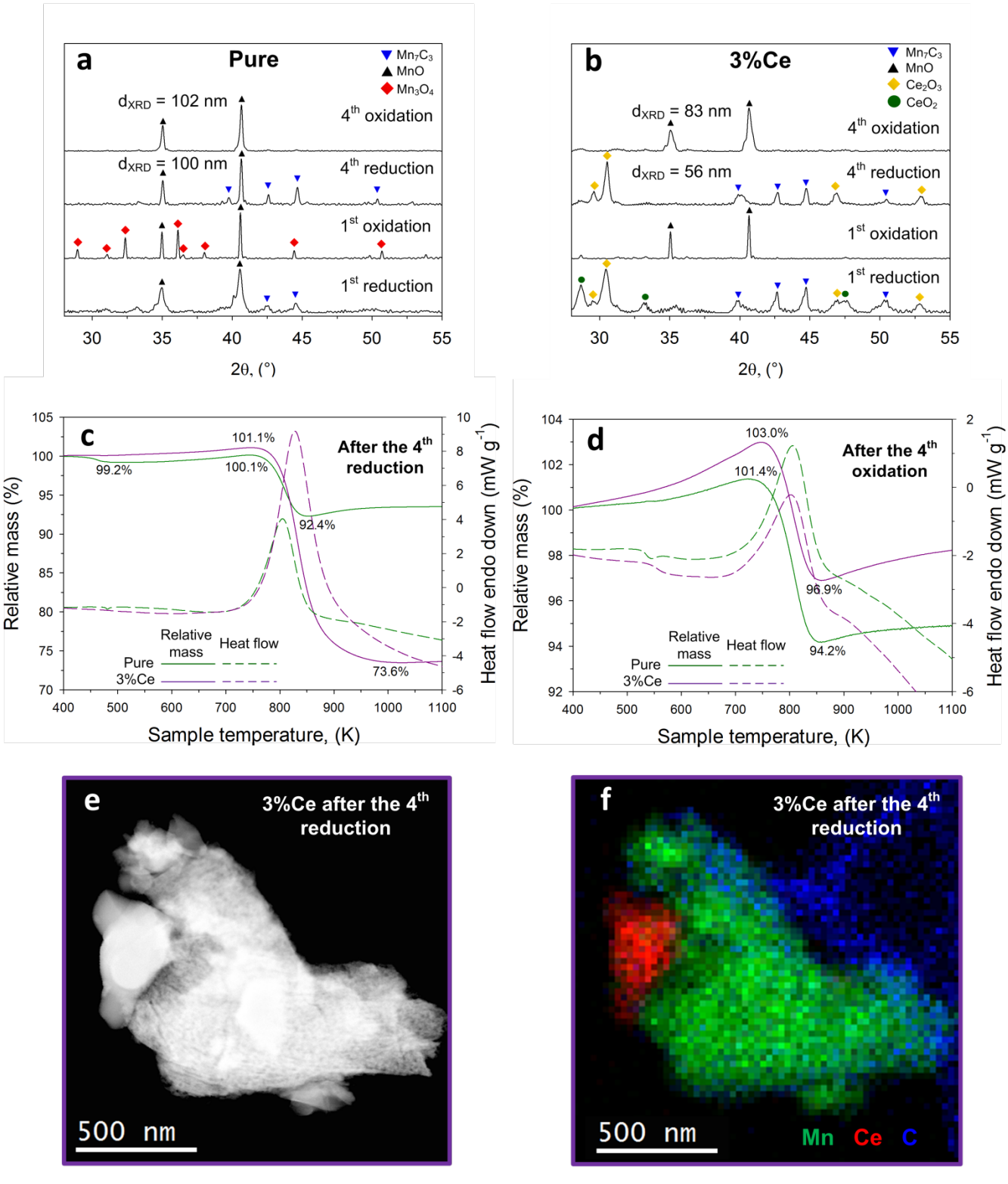
a
Pure
Mn_7C_3
MnO
Mn_3O_4
d_{XRD} = 102 nm
4th oxidation
d_{XRD} = 100 nm
4th reduction
1st oxidation
1st reduction
2θ, (°)
b
3%Ce
Mn_7C_3
MnO
Ce_2O_3
CeO_2
d_{XRD} = 83 nm
4th oxidation
d_{XRD} = 56 nm
4th reduction
1st oxidation
1st reduction
2θ, (°)
c
After the 4th reduction
101.1%
99.2%
100.1%
92.4%
73.6%
Relative mass
Heat flow
Pure
3%Ce
Relative mass (%)
Heat flow endo down (mW g-1)
Sample temperature, (K)
d
After the 4th oxidation
103.0%
101.4%
96.9%
94.2%
Relative mass
Heat flow
Pure
3%Ce
Relative mass (%)
Heat flow endo down (mW g-1)
Sample temperature, (K)
e
3%Ce after the 4th reduction
500 nm
f
3%Ce after the 4th reduction
500 nm
Mn Ce C

Figure 4

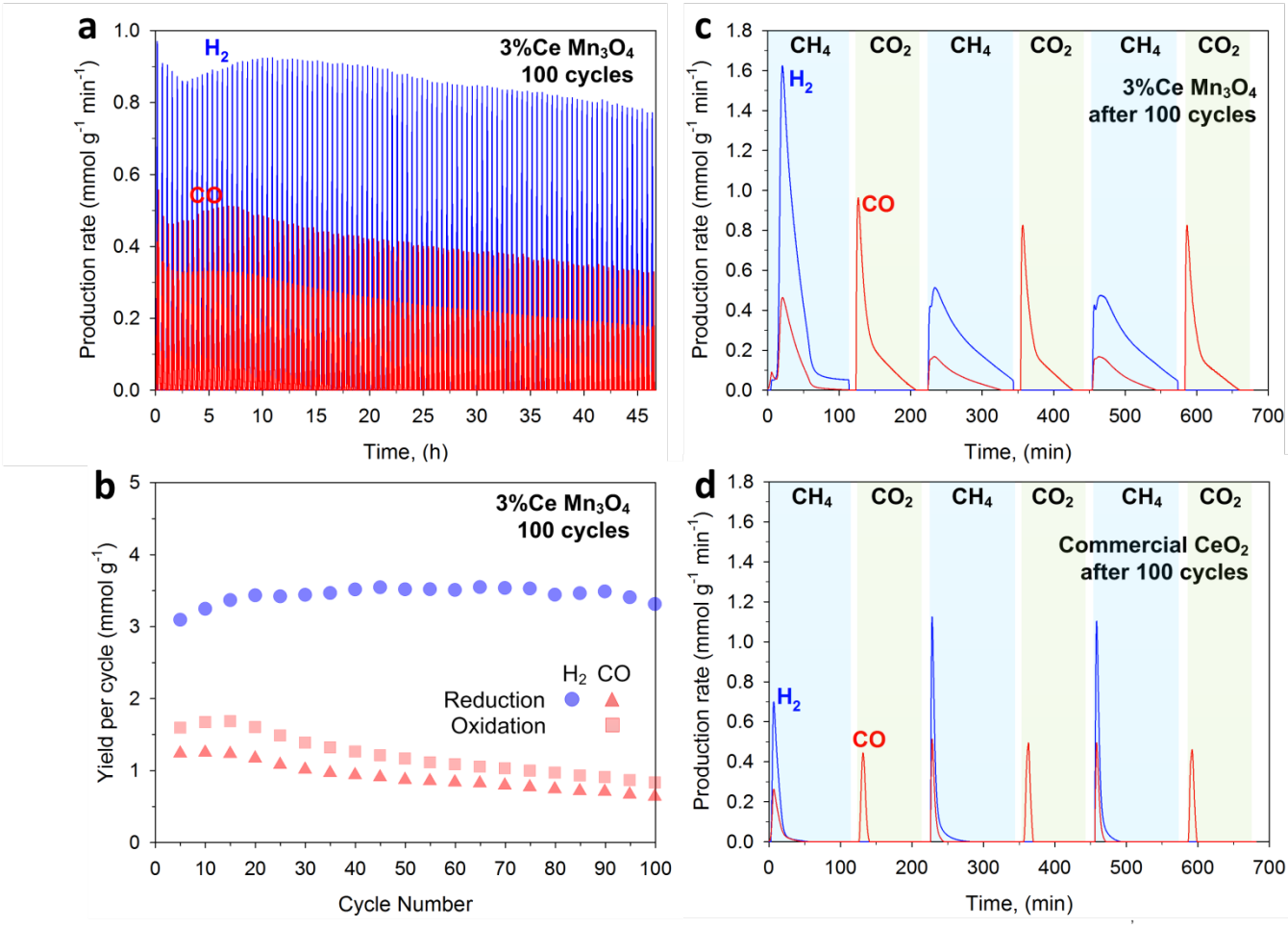
a
H2
CO
3%Ce Mn3O4
100 cycles
Production rate (mmol g-1 min-1)
Time, (h)
b
3%Ce Mn3O4
100 cycles
H2 CO
Reduction
Oxidation
Yield per cycle (mmol g-1)
Cycle Number
c
CH4 CO2 CH4 CO2 CH4 CO2
H2
CO
3%Ce Mn3O4
after 100 cycles
Production rate (mmol g-1 min-1)
Time, (min)
d
CH4 CO2 CH4 CO2 CH4 CO2
Commercial CeO2
after 100 cycles
H2
CO
Production rate (mmol g-1 min-1)
Time, (min)

Figure 5